Journal of Materials Chemistry A

Accepted Manuscript

ROYAL SOCIETY OF CHEMISTRY

www.rsc.org/materialsA

Journal of Materials Chemistry A

ARTICLE

The Preparation and Properties of Carbon Inverse Opal Papers Using Carbon Fiber Sheets as a Framework

Received 00th January 20xx,
Accepted 00th January 20xx

DOI: 10.1039/x0xx00000x

www.rsc.org/

Justin C. Lytle,[*a] Julian M. Banbury,[a] Rebekah A. Blakney,[a] Michaela S. Burke,[a] Ryan P. A. Clark,[a] Robert D. Fisher,[a] Sally V. Frederiksen,[a] Ashley R. Marshall,[a] Marshall T. McNally,[a] Morgan L. Ostendorf,[a] Kelsey N. Serier,[a] Michael Shiu,[a] Ryan E. Toivola,[b] Chelsea S. Travers,[a] and Erin R. Wright[a]

Carbon inverse opal monoliths store energy, sense small molecules, and catalyse reactions, but can be limited by their rigid form because it prevents the mechanical flexure that would be needed to embed this material within devices that bend during use. We report a method that uses carbon fiber papers to impart partial mechanical flexibility and greater electronic conductivity to carbon inverse opals. Our approach deposits colloidal crystals between the fibers in carbon fiber paper and uses the colloidal crystal templates to form inverse opal carbon from phenolic resin. The resulting carbon inverse opal papers (CIOPs) comprise both three-dimensionally interconnected macropores and aperiodic meso- and micropores, the combination of which establishes hundreds of square meters of interfacial area per gram that can store and discharge electrochemical capacitance while planar, while flexed around radii of curvature as small as 5 mm, and after 150 reversible flexures. Carbon inverse opal papers offer at least 3 times greater electronic conductivity than reported carbon inverse opals because the network of carbon fibers doubly serves as pliable framework and conductive conduit.

Introduction

Porous carbon nanomaterials are lightweight, relatively inexpensive, electrically conductive, and can have interconnected pore networks that make it possible for chemical and electrochemical fluxes to simultaneously access their abundant interfacial areas.[1-3] In spite of these attributes, many types of nanostructured carbon are formed as rigid objects that are not adaptable, without further modifications, to devices that require flexure, such as wearable electronic tags and multifunctional fabrics that synergistically combine power harvesting, storage, and computing capabilities.[4] Elastomeric binders and other additives have been blended with porous carbons to give the resulting composites a greater degree of flexibility than in their as-prepared form, but those approaches typically require nanostructured carbons to be milled into fine powders.[5]

Carbon inverse opal monoliths[6] (CIOMs) are one such example of an inflexible porous carbon that has been explored as an electrode material for Li-ion batteries[7,8] and capacitors,[9] as well as for applications in sensing[10] and catalysis.[11] Typically, CIOMs are prepared by assembling monodisperse colloids, which range from tens to hundreds of nanometers in diameter, into close-packed crystalline arrays. The void spaces between colloids are subsequently infiltrated with polymeric or other hydrocarbon precursor solutions or vapors.[12,13] These composite materials are pyrolyzed at elevated temperatures to thermally decompose the polymer colloids and to carbonize the substances that occupy the voids in the colloidal crystal template. The resulting carbon-based monoliths comprise spherical, three-dimensionally interconnected pores; this pore network has the inverse structure of the original colloidal crystal template.[12,14] However, like many porous carbons, CIOMs are physically inflexible under applied force because hard carbons are inherently rigid and nanostructured pore walls are themselves delicate.[13,15] Our work seeks an alternative route to fabricate CIOMs that are capable of greater flexibility without requiring elastomeric binders.

The modest electronic conductivity of porous carbon nanomaterials can further limit their utility.[6,7] The flow of electronic charge in porous carbons is impeded by the low-density network of their conductive pathways and by the microstructure of hard carbon itself. For example, CIOMs prepared from phenolic precursors typically exhibit σ_{elec} < 1 S cm^{-1} and at best display 10 S cm^{-1}. Therefore, increasing the electronic conductivity of porous carbon electrodes is critical to create nanomaterials that can handle larger current densities and more efficiently dissipate heat.

With these needs in mind, we report a method to prepare carbon inverse opals that are more flexible and conductive than conventional CIOMs. This method fabricates carbon inverse opals within the void spaces in carbon fiber papers; the

[a] Chemistry Department, Pacific Lutheran University, 12180 Park Ave S, Tacoma, WA 98447 USA. E-mail: lytlejc@plu.edu
[b] Department of Materials Science and Engineering, University of Washington, 302 Roberts Hall, Seattle, WA 98195 USA.

resulting carbon inverse opal papers (CIOPs) can be flexed over a moderate range of curvature and transport electronic and electrochemical charges to and from the individual domains of carbon inverse opals. We demonstrate in this work that CIOPs have abundant interfacial areas that reversibly store and discharge electrochemical capacitance while being moderately flexed and after many flexures. To the best of our knowledge, carbon inverse opals have not previously been integrated into carbon fiber papers, although fabrics,[16-18] carbon fiber papers,[3,19,20] and nanotubes[21-24] have previously been used to impart flexibility and/or conductivity throughout polymers, carbons and inverse opal metal oxides. Other researchers have demonstrated that spherical colloids can be electrosorbed as colloidal crystals on individual carbon fibers,[25] and that silk cloths can serve as a soft substrate upon which colloidal crystals and inverse opals can be deposited as photonic crystal materials.[26]

Experimental

Synthesis of monodisperse spherical colloids

Monodisperse spherical poly(methyl methacrylate) (PMMA) colloids were prepared using an established free-radical polymerization method.[27] Monomethylether hydroquinone stabilizer was first extracted from methyl methacrylate (MMA, Sigma–Aldrich, <99%) via successive washes in aqueous sodium hydroxide solution; inhibitor-free MMA was dried over anhydrous sodium sulfate and was refrigerated in an amber-colored bottle until use. A mixture of 200 mL of MMA and 750 mL of water (purified to ~18 MΩ cm) was simultaneously stirred at ~300 rpm, degassed by bubbling Ar(*g*) through the emulsion, and heated to 80 ˚C. The polymerization reaction was initiated by adding a 50-mL aqueous solution that contained 0.5 g 2,2'-azobis (2-methylpropionamidine) dihydrochloride (Sigma–Aldrich, 97%), and the resulting white colloidal suspension was filtered through glass wool after the reaction was complete. This synthesis produced spheres with a diameter of 250±10 nm, according to electron micrograph measurements of a minimum of ten spheres from multiple regions in each sample.

Assembling colloidal crystal papers

Monodisperse polymer and silica spheres have previously been formed into colloidal crystal monoliths by centrifuging or sedimenting sphere suspensions,[28] and also into thin films by controllably evaporating the suspending fluid from a suspension.[29,30] We modified this latter approach to assemble spheres into close-packed colloidal crystals that occupy the interfiber voids in carbon fiber papers.

Individual pieces (1 cm × 2 cm) of Lydall Technimat carbon fiber paper (~100 µm thick) were sandwiched between two glass microscope slides, such that 2 mm of the paper protruded as a wick that induces the aqueous PMMA suspension to enter the papers through capillary uptake. This

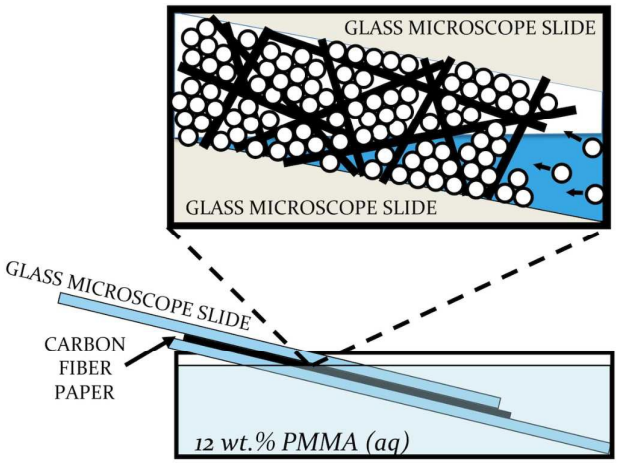

Fig. 1 A schematic diagram of the setup that deposited monodisperse spheres as colloidal crystals within carbon fiber papers.

assembly of glass slides and carbon fiber paper was nested at an angle of ~10˚ in a glass Petri dish (Fig. 1). Each dish was filled with a ~12 wt.% suspension of monodisperse PMMA colloids and was heated at 35 ˚C on a hotplate to gradually evaporate the aqueous suspension, thereby driving the crystallization process over the course of 48 h. After the opal papers were dry, they were heated at 113 ˚C for 15 minutes in a Lindberg Blue M tube furnace to anneal the PMMA spheres into a cohesive network of fused spheres that remained integrated during subsequent infiltration with a structure-forming polymeric precursor solution.

Fabricating carbon inverse opal papers

A resorcinol-formaldehyde (RF) precursor was subsequently infiltrated into the interstitial voids between spheres in each colloidal crystal paper.[6,7,12] In a typical synthesis, 15.0 g (136 mmol) of resorcinol (Sigma-Aldrich, 99%), 0.288 g (2.71 mmol) of anhydrous sodium carbonate (Baker Chemical Co., 99.9%), and 22.11 g (273 mmol) of aqueous formaldehyde solution (Sigma-Aldrich, 37 wt.%) were mixed until dissolved in a sealed jar. Four drops of this solution were applied via pipette to a colloidal crystal paper that was supported on a single glass microscope slide. The wetted papers were covered with a second glass slide, and the ends of the slides were gently fixed together with binder clips, such that the clips did not apply pressure directly onto the samples. Each assembly was sealed in a Nalgene bottle and heated at ~90 ˚C in a Nesco pressure cooker for 9.5 hours in order to cure the RF polymer. The RF-PMMA paper composites were subsequently pyrolyzed in a tube furnace with flowing $N_2(g)$ at 1000 ˚C (2 ˚C min^{-1} heating ramp), during which time the RF polymer decomposes into hard carbon and PMMA depolymerizes into molecular fragments that are carried away in the gas stream.

Characterization

All PMMA colloids and ClOPs were imaged using a JEOL 7000 field-emission scanning electron microscope. Colloidal crystal papers and ClOPs were cross-sectioned using clean razor blades. All carbon samples were mounted on aluminum stubs using conductive carbon tape and were viewed without sputter coating. Colloidal crystal papers were mounted using conductive tape as above, and were sputtered with ~10 nm of Pt. Individual PMMA sphere diameters were measured by applying one drop of PMMA colloidal suspension to an aluminum stub. The suspension was dried and the resulting solid was sputtered with ~10 nm of platinum to reduce beam charging artifacts during imaging. All micrographs except that shown in Fig. 2A were captured as cross-sections to observe the porosity of sample interiors.

The presence, abundance, and size distribution of micropores, mesopores, and macropores in ClOPs were characterized using nitrogen physisorption porosimetry and mercury intrusion porosimetry. Nitrogen adsorption/desorption isotherms were measured on a Micromeritics ASAP2010 porosimeter. The distribution of larger macropores was determined by mercury intrusion porosimetry, which was measured with a Micromeritics Autopore IV 9500 using a penetrometer stem with 0.392 cm^3 of intrusion volume.

The mechanical properties of ClOP sheets were tested with a Perkin Elmer dynamic mechanical analyser 7e using a three-point bending configuration. A 15-mm span supported individual ClOP sheets (~20 mm × ~7 mm × 0.08 mm) as a static force of 20 mN was initially applied by a knife-edged probe along the ~7-mm width of each sample; the applied force was increased by 10 mN min^{-1} until fracture. The instrument was programmed using Pyris software.

The electronic conductivity values of planar carbon fiber papers and ClOPs were measured and calculated using a four-point technique that was established by van der Pauw.[31]

All electrochemical testing was performed with a Gamry Reference 600 potentiostat using a three-electrode cell configuration. Carbon inverse opal paper working electrodes (1 cm × 1 cm) were secured in Dexmet nickel mesh as a current collector and were cycled against a reticulated vitreous carbon foam counter electrode. The electrochemical capacitance of ClOP electrodes was measured by cyclic voltammetry and galvanostatic cycling in 2.5 M Li_2SO_4(*aq*) after the electrodes had been vacuum infiltrated with electrolyte for at least 1 h. Cyclic voltammetry measurements were acquired between -0.2–0.8 V (vs. Ag/AgCl) using scan rates that ranged from 1–100 mV s^{-1}. Galvanostatic measurements were acquired within the same potential limits using a range of mass-normalized currents (0.5–2.0 A g^{-1}). The specific capacitance of each electrode was calculated by dividing the current (in Amperes) during galvanostatic discharge by the mass of the electrode and the slope of the first half of the galvanostatic discharge curve, as described by Stoller *et al.*[32] Impedance spectra were subsequently measured by applying a direct current bias of 0.2 V over a frequency range from 0.01–1×10^6 Hz. Bode plots of the ClOP's imaginary capacitance were generated using the guidelines that were stated by Taberna *et al.*[33]

The electrochemically accessible surface area of ClOPs was estimated via cyclic voltammetry in a nonaqueous electrolyte of 0.1 M tetrabutylammonium perchlorate (TBAP, Sigma–Aldrich, ≥98%) in acetonitrile. In these cases, ClOP working electrodes were vacuum infiltrated with this nonaqueous solution for 1 hour prior to measurement in order to fully wet the carbon's pore network. All nonaqueous measurements utilized reticulated vitreous carbon foam as the counter electrode and a nonaqueous reference electrode (BASi Analytical) that contained a Ag wire in 10 mM $AgNO_3$ and 0.1 M TBAP in acetonitrile. The electrochemically accessible surface area of ClOPs was estimated from the magnitude of electrochemical capacitance that was discharged during cyclic voltammetry at 1 mV s^{-1} between 0.2–0.8 V.[3] Electrochemical surface areas were calculated by dividing the average magnitude of current discharged between 300–700 mV by the scan rate (in Volts per second) and the mass of the carbon electrode. This calculation is based on the accepted capacitance value of 10 μF cm^{-2} for carbon electrodes in 0.1 M TBAP in acetonitrile.[3]

The amount of electrochemical capacitance that was discharged by ClOP electrodes at various degrees of flexure was estimated from cyclic voltammetry in 0.1 M TBAP in acetonitrile. The 1 cm × 1 cm ClOP sheets for this measurement were individually contained in Ni mesh current collectors and these electrode assemblies were flexed around cylindrical objects that had diameters between 10–95 mm. These ClOP electrodes retained the imposed flexures while they were electrochemically cycled between 0.2–0.8 V at 1 mV s^{-1} in a three-electrode configuration.

Likewise, the same electrode assemblies were repeatedly flexed to determine whether mechanical fatigue affects the amount of capacitance that ClOP electrodes discharge. In this test, planar ClOP electrode assemblies were flexed around a cylindrical object with a 25-cm diameter. The electrodes were subsequently flipped over and flexed again in the reverse direction around the same cylinder. Each ClOP was flexed a total of 150 times in this fashion, and the electrochemical capacitance was subsequently measured in 0.1 M TBAP in acetonitrile as above.

Results and discussion

Physical properties of Lydall carbon fiber paper

Lydall carbon fiber papers comprise randomly interleaved carbon fibers that are ~10 μm in diameter (Fig. 2A). The disperse assembly of fibers in the paper creates interfiber voids on the order of tens to hundreds of micrometers, and it is within these voids that PMMA colloids deposit to form close-packed templates.

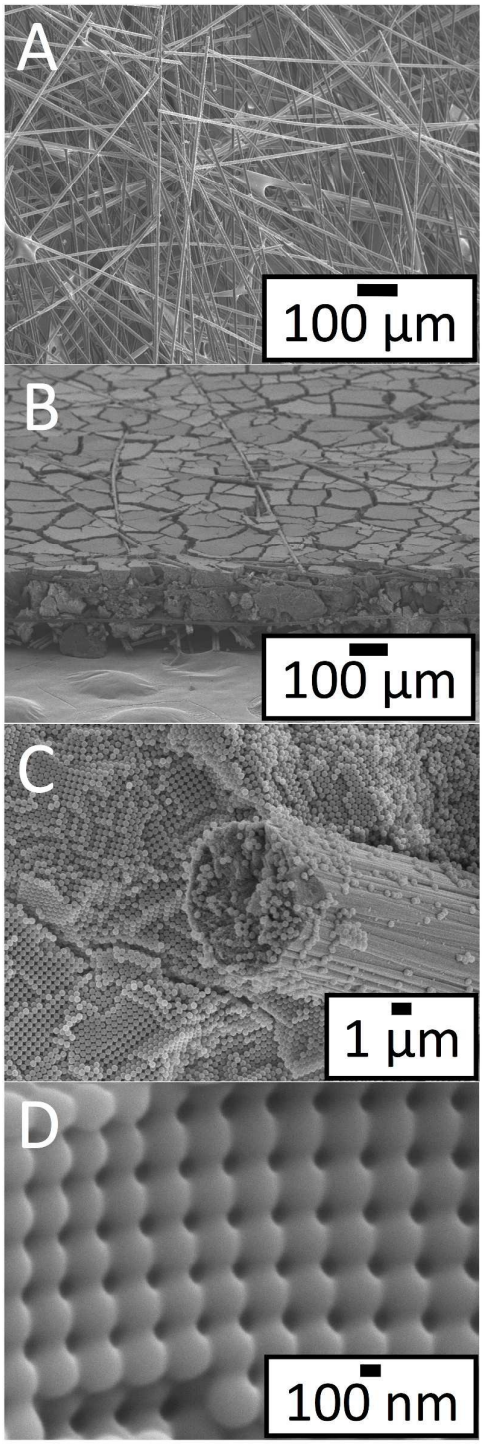

Fig. 2 Scanning electron micrographs of (A) an as-received carbon fiber paper; (B) the high degree of interfiber volume-filling in a colloidal crystal paper; (C) close-packed colloidal spheres surrounding a carbon fiber in the paper; and (D) interparticle connections between PMMA colloids after thermal annealing.

Structural properties of colloidal crystal papers

The colloidal crystal papers prepared by this method appear faintly opalescent because the spheres in close-packed regions of the sample have a periodicity that diffracts visible light. At low magnifications of electron microscopy, the void volume in each carbon fiber paper appears to be occupied by colloidal spheres that accumulated as the meniscus of the colloidal suspension retreated during the evaporative deposition process (Fig. 2B). Mud cracks and planar defects exist in the colloidal crystal papers between domains of spheres that are ~100 µm in size. Similar structural defects are commonly observed in colloidal crystal films.[29,30]

At higher magnifications, most of the regions in colloidal crystal papers appear to be a collection of polycrystalline domains that comprise close-packed monodisperse (250±10 nm) PMMA spheres (Fig. 2C). Necks are present between the polymer spheres after thermal annealing, which helps spheres to remain stationary as RF precursor solution is subsequently infiltrated to prepare ClOPs (Fig. 2D). Some regions of these samples contain spheres that assembled into aperiodic packing geometries. Packing defects are common in colloidal crystals, and while it is possible to decrease the density of defects in colloidal crystals,[29] it is nontrivial to avoid them altogether in planar geometries and is especially challenging within a matrix of randomly interleaved carbon fibers. Unlike photonic band gap materials that have strict tolerances for defects, though, porous electrodes for energy storage and catalysis applications would continue to function when they comprise disordered pore geometries so long as chemical and electrochemical flux lines extend throughout the entire pore network and the active electrode materials remain electrified in a circuit.[3]

Morphology of carbon inverse opal papers

After colloidal crystal papers are infiltrated with RF solution, cured, and pyrolyzed, the ensuing solids are black sheets that are filled to a high degree with porous carbon nanoarchitectures between the fibers in the paper (Fig. 3A). Fissures are present in the RF-derived carbon where mud cracks and other structural defects previously existed in the template and where the material outgassed and densified during pyrolysis. A slow heating ramp (2 ˚C min^{-1}) during pyrolysis reduces the rate of outgassing and densification and thereby minimizes strain within the material during thermal processing.

At higher magnifications, the inverse opal pore structure is visible in approximately 50–75% of the regions in these samples. The three-dimensionally ordered macropores within these regions have a diameter of 207±25 nm (Fig. 3B) and are arranged in polycrystalline close-packed domains that span several micrometers. The macropores in inverse opal domains connect in three dimensions to neighboring sphere cavities through pore windows that exist where PMMA spheres previously were in contact with each other. The remaining regions of RF-carbon nanomaterials comprise aperiodic

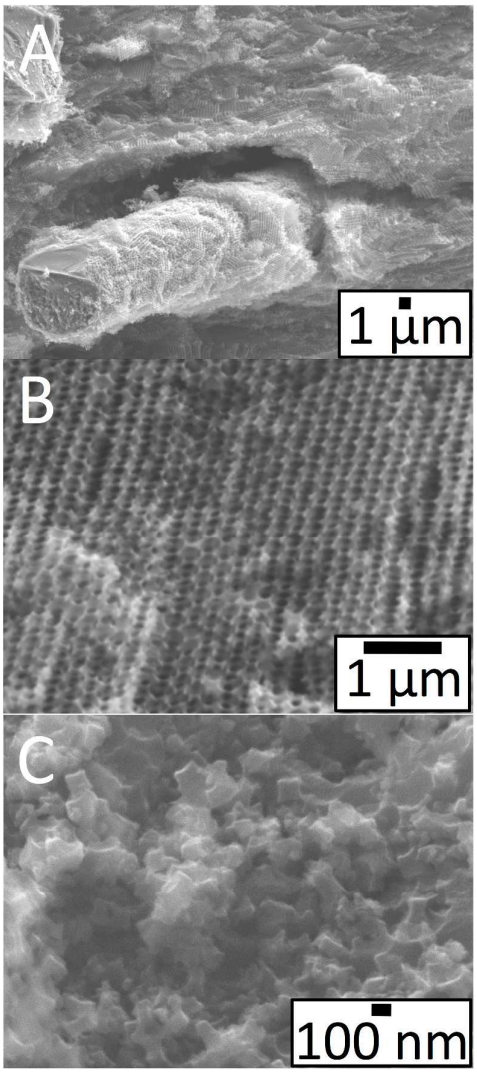

Fig. 3 Scanning electron micrographs in the cross-section of a CIOP sample: (A) carbon inverse opal domains surrounding a carbon fiber; (B) close-packed planes of macroporous voids in a CIOP; and (C) a region of aperiodic porosity in a CIOP sample.

mesopores and macropores (Fig. 3C) that were templated by disordered regions in the colloidal crystal papers. Although we routinely blotted excess RF solution from the surface of colloidal crystal papers using tissues, the surface of each CIOP is sometimes partially covered in a skin of non-templated RF-carbon that ranges in thickness from hundreds of nanometers to a few micrometers. We attribute these crusts to chemical interactions between the RF solution and surface groups on glass microscope slides, as well as to any pooling of RF precursor that would occur at nonplanar regions of the slides and carbon fiber paper.

Pore networks in carbon inverse opal papers

We assessed the surface areas and pore sizes in CIOPs via nitrogen physisorption, mercury intrusion, and electrochemical surface area measurements. Of the 34 CIOP samples that we prepared, there was a broad range of electrochemical surface areas that varied from <100 $m^2 g^{-1}$ to >400 $m^2 g^{-1}$, with 50% of all CIOP samples having <200 $m^2 g^{-1}$. Because such a wide range of electrochemical surface areas was determined for CIOPs, we sought another estimate by measuring the sorption characteristics of a collection of twenty CIOPs during one nitrogen porosimetry experiment. Carbon inverse opal papers exhibit type II sorption isotherms that are characteristic of macroporous sorbents and have a slight hysteresis that is associated with narrow slit-shaped pores that form between particles as textural porosity (Fig. 4A).[34] The Brunauer-Emmett-Teller (BET) specific surface areas of CIOPs were estimated from nitrogen sorption measurements to be 190 $m^2 g^{-1}$ (Table 1), which is nearly identical to the 50th percentile of our electrochemical surface area data. We interpret the ensemble of micrographic, electrochemical and sorption data to mean that while inverse opal macropores are abundantly present in the samples, the additional aperiodic pore structures in CIOPs can be highly variable, and that the average pore structure in CIOPs has approximately 190 $m^2 g^{-1}$ of specific surface area.

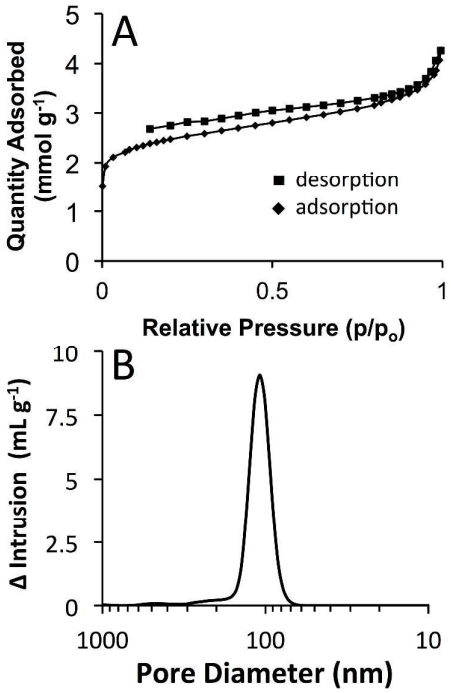

Fig. 4 A nitrogen sorption isotherm (A) and mercury intrusion pore size distribution (B) that were measured from CIOP samples.

Table 1 Summary of nitrogen sorption and mercury intrusion porosimetry measurements of CIOPs.

BET surface area ($m^2 g^{-1}$)[a]	t-plot micropore surface area ($m^2 g^{-1}$)[a]	cumulative pore volume ($cm^3 g^{-1}$)[a]	total intrusion volume ($cm^3 g^{-1}$)[b]	bulk density ($g\ cm^{-3}$)[b]
190	127	0.11	2.5 ± 0.1	0.30 ± 0.02

[a] determined from nitrogen porosimetry of twenty CIOPs that were simultaneously analyzed in one sorption experiment

[b] determined from Hg intrusion porosimetry of four CIOPs. Each batch of four CIOPs was measured collectively in order to occupy a minimum 20 vol.% of the penetrometer bulb.

Although nitrogen porosimetry is commonly used to determine the specific surface areas of porous solids, mercury intrusion porosimetry more accurately determines the pore size distribution in the macropore regime. According to mercury intrusion measurements, the majority of pore volume in CIOPs corresponds to macropores that are ~100 nm in diameter, with a minor contribution of pore volume from inverse opal macropores that are ~200 nm in diameter (Fig. 4B). We attribute the ~100 nm macropores to regions in CIOPs that either buckled under the pressure of the intruding mercury or were templated by spheres which deposited aperiodically between the randomly assembled carbon fibers. Even though inverse opal macropores were observed by SEM to exist in the majority of regions in our samples, the ~100 nm aperiodic pores make up the majority of the pore volume in CIOPs because there are cumulatively a greater number of them. Similar ~100 nm aperiodic macropores have previously been observed for carbon nanofoams that were prepared using similar precursors: polyacrylonitrile carbon fiber papers, base-catalyzed RF chemistry, and glass microscope slide containers.[3] Under these conditions, some regions of disordered aerogel-like mesopores and macropores form between carbon fibers and also in structural defects in the colloidal crystal papers where polymer spheres did not deposit.

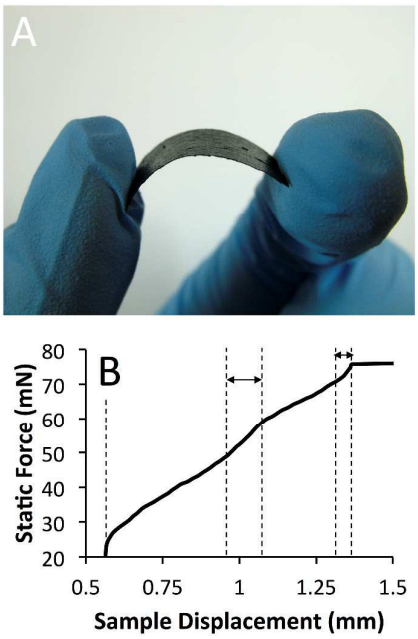

Fig. 5 A photograph (A) that demonstrates the degree of mechanical flexure that is possible in CIOPs. A static force curve (B) of the three-point bending motion of a representative CIOP sheet that was tested via dynamic mechanical analysis. The material's pseudo-linear response to static force is denoted between the dashed vertical lines.

Mechanical properties

Mechanical flexure is a critical design parameter to consider when preparing porous materials for devices that must conform to bodies in motion, such as smart textiles[35] or other wearable technology.[36] Individual CIOPs reversibly flex when force is applied (Fig. 5A); we quantified this mechanical property of individual CIOP sheets using three-point bending tests with a dynamic mechanical analyser. The CIOP sheets have an average flexural strength of 38±12 MPa at the fracture point of the material, at which the midpoint of the sheets extends 2.5±0.6 mm below the plane of the span. This deflection at fracture corresponds to a radius of curvature of 13±4 mm and spans a central angle of 73±23˚. Radii of curvature have previously been reported as an important metric when establishing the flexibility of carbon-based sheets.[37] The flexural strength of CIOPs ranged from 15–51 MPa in the seven samples that were measured, and we interpret this deviation to indicate that the random orientation and density of fibers in CIOP papers creates anisotropic flexural properties. For comparison, Lydall carbon fiber papers elastically bend but do not fracture under the same testing conditions. As expected, the carbon fiber framework is the source of flexibility in CIOPs, and the inelastic carbon inverse opal domains within the fiber matrix limit the flexure of CIOPs.

Further insight into the flexural properties of CIOPs is gained by analysing each CIOP's static force curve as the material is bent by the mechanical analyser. After a 20-mN force is initially applied to each sheet, the static force curves of CIOPs exhibit a saw-tooth shape as additional force is applied at a rate of 10 mN min^{-1} (Fig. 5B). We interpret this pseudo-linear behaviour to mean that static forces are not uniformly distributed throughout the non-homogeneous composite of carbon fibers and carbon inverse opal domains during flexure. For example, relatively little force is needed to bend CIOPs during some points in each measurement, which implies that the carbon fibers within are able to slide past each other without great resistance at some when flexure. These regions correspond to the shallow slopes that are visible in the static force curve. In contrast, steeper slopes in the static force curve correspond to instances when the CIOP stiffens as its carbon fibers are pinned by other fibers and by other domains of inverse opal carbon.

While CIOPs are not completely elastic and cannot be folded or aggressively twisted, they enable carbon inverse opals for the first time to reversibly conform to moderate flexural deformations, even during electrochemical cycling (see the following section on *Electrochemical behavior*). In contrast, many common porous materials, including CIOMs, are rigid and fracture rather than bend when sufficient external force is applied.[13] For this reason, many types of porous materials for energy storage applications have been blended with polymeric binders, cross-linking agents,[38] graphene additives,[39] and carbon fiber papers[3,19,20] to create composites that achieve similar or greater flexibilities as CIOPs.

Electronic conductivity

Not only is flexure an essential design consideration for diverse electronics applications that are miniaturized and/or wearable, but so too is the electronic conductivity of a material a

measure of its suitability for energy storage devices and electrocatalysis. Ideally, one would measure the change in the four-point electronic conductivity of the CIOPs as a function of their degree of flexure, but it was nontrivial to acquire this data because doing so meant placing sufficient pressure on the corners of the CIOPs to cause physical damage to the sample during flexure. We measured the four-point electronic conductivity of flat CIOPs to be 33±2 S cm^{-1},[31] which is at least 3 times greater than that of previously reported CIOMs.[6,7] We attribute this increase in conductivity to: (1) carbon fibers that transport electrons throughout CIOPs as conductive conduits (6±3 S cm^{-1}); (2) regions of inverse opal carbons and disordered porous carbons that create conductive pathways between carbon fibers; and (3) domains that consist of nontemplated carbons on or within the material. The conductivity of CIOPs is in the range reported for carbon nanofoams (20–200 S cm^{-1}),[3] which also integrate porous, but aperiodic, carbon nanostructures within flexible and conductive sheets of carbon fiber paper.

Electrochemical behavior

The aggregate physical and electrochemical properties of carbon fiber papers and carbon inverse opals create a hybrid material that stores and discharges electrochemical energy. Carbon fiber papers are themselves flexible and electronically conductive, and the carbon inverse opal pore structure comprises an interconnected pore network with abundant interfacial area (~100s m^2 g^{-1}). This ensemble of attributes enables CIOP electrodes to discharge tens of farads of electrochemical capacitance per gram of CIOP (as-prepared, unbent) when cycled at 1 mV s^{-1} in 2.5 M Li_2SO_4(*aq*) electrolyte solution (Fig. 6A). While it was not possible to determine a representative specific capacitance value for CIOPs because they exhibit a wide range of specific surface areas, the range of electrochemical capacitance values that are discharged by CIOPs (14–47 F g^{-1}) overlaps with and includes the 30 F g^{-1} that was reported by Fischer et al. for analogous carbon nanofoam electrodes, which were prepared using similar precursors and carbon fiber papers and that were electrochemically tested under similar conditions.[40] Considering that approximately two-thirds of the mass in each CIOP sheet is made up of carbon fibers—which themselves have <1 m^2 g^{-1} of surface area and therefore contribute little to the specific capacitance of CIOP electrodes—the nanostructured domains in CIOPs are the primary source of the capacitance seen in these measurements. By normalizing the specific capacitance of CIOPs only to the mass of the electrochemically active porous carbon domains, these domains discharge a wide range of capacitance values (~42–141 F g^{-1} in 2.5 M Li_2SO_4(*aq*)) that overlaps the range of capacitance values that has been reported for other porous carbons (typically 100–120 F g^{-1} in neutral electrolyte).[41] Greater electrochemical capacitance (150–250 F g^{-1}) is possible for a variety of high-surface-area carbons (graphenes, nanotubular carbons, and carbon nanofibers) that are cycled in acidic or alkaline aqueous electrolytes.[42,43]

Cyclic voltammetry measurements demonstrate that as-prepared, unbent CIOP electrodes store and discharge electrochemical energy as pseudocapacitance in aqueous electrolyte (Fig. 6A). Pseudocapacitance in hard carbons has been ascribed to redox-active ether and alcohol functionalities that are known to exist at the double-layer interfaces of RF-derived carbons.[44] The presence of these functional groups does not degrade the electrochemical performance of CIOPs upon repeated cycling. Instead, CIOP electrodes retain their electrochemical capacitance over 1,000 cycles (Fig. 6B) and gain ~5% additional capacitance in the process, which is likely caused by polar and/or redox-active groups that form on the porous carbon walls during repeated cycling.

The shape of the cyclic voltammograms for CIOP electrodes gradually changes from being nearly flat at slow scan rates that approximate electrochemical equilibrium (1 mV s^{-1}) to being increasingly polarized when CIOP electrodes are cycled at 100 mV s^{-1}. Electrochemical polarization is commonly encountered in porous carbon electrodes when they are cycled faster than the rate at which charged species can diffuse through pore networks.[45] Likewise, electrodes can also polarize when the charge-transfer kinetics of Faradaic processes at an electrode's surface cannot keep up with the cycling rate.

Carbon inverse opal paper electrodes (in nickel mesh) electrochemically cycle while they are flexed over a curved substrate. Carbon inverse opal papers in nickel mesh current collectors can be elastically flexed without sustaining visible physical damage when curved around cylindrical objects with a radius of curvature of as little as 5 mm (115° central angle of curvature). Future studies could evaluate the contribution of Ni mesh and other current collecting substrates to the degree of flexure in pliable electrode materials. Three separate CIOP

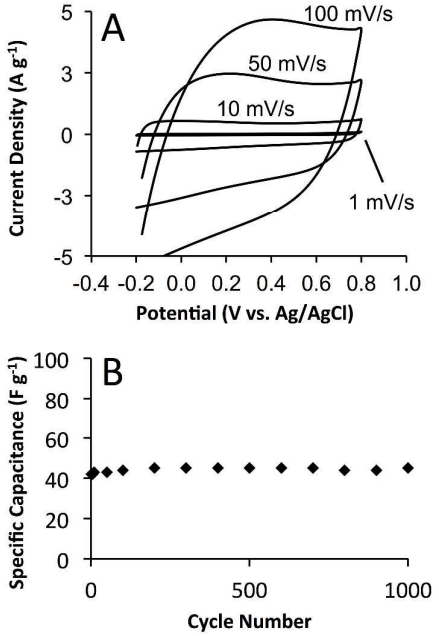

Fig. 6 (A) Cyclic voltammograms (top) of CIOP electrodes at scan rates of 1, 10 50, and 100 mV s^{-1} in 2.5 M Li_2SO_4(*aq*). (B) A plot of the cycling stability of a representative CIOP electrode over 1000 cycles in 2.5 M Li_2SO_4(*aq*) (-0.2–0.8 V vs. Ag/AgCl).

electrodes (in nickel mesh current collectors) were electrochemically cycled in 1 M TBAP/acetonitrile while flat and then over cylindrical objects with increasingly smaller diameters. The electrochemical specific capacitance of these samples initially decreased by 5–28% when they were curved over a cylindrical object with a diameter of 95 mm (which corresponds to a central angle of 12˚, Fig. 7A).

We attribute this decrease to the initial repositioning of carbon fibers and carbon inverse opal domains within the samples, which would alter the pathways for electronic current to flow and could electrochemically deactivate some inverse opal domains. However, the specific capacitance of CIOPs subsequently increased when flexed over objects of even greater curvature. When CIOPs are curved around a cylinder with a diameter of 10 mm (115˚ central angle), they discharged 92–118% of the amount of specific capacitance that they discharged when flat. We interpret this to mean that the carbon fibers and domains of nanostructured carbon acquire better electronic contact as they flex to greater curvatures, which concurs with our interpretation of the static force curve (Fig. 5B) that CIOP become increasingly stiff when flexed.

As another measure of CIOPs moderate flexibility, the same CIOP electrode assemblies were curved forward and backward for a total of 150 flexures around a cylindrical object (25-mm diameter, 46˚ central angle) to determine whether and how the electrochemical capacitance of the material responds to repeated flexure. Two of three CIOP samples retained >86% of their electrochemical capacitance after 150 flexures (Fig. 7B), whereas the capacitance of the third CIOP sample retained just 43% after 150 flexures. We attribute the latter to the partial disintegration of the interwoven carbon fiber matrix and/or domains of porous carbon. Collectively, this data confirms that CIOPs can reversibly flex, forward and backward, over an object of moderate curvature and maintain 43–86% of their capacitance after 150 flexures. It is clear that CIOPs are not as elastic as composite electrode blends that contain elastomeric binders, nor are they as elastic as bulk textiles that have been coated with carbon nanotube slurries.[46] Still, this method results in a moderately flexible and conductive form of carbon inverse opal that is in distinct contrast with the rigid monolithic form of carbon inverse opal that has precedent in the literature.

Beyond testing the mechanical and electrochemical properties of CIOPs under flexural strain, there are three additional pieces of evidence that the carbon inverse opal domains are reasonably well integrated into the carbon fiber framework. Firstly, the electronic conductivity of CIOP sheets is greater than that of its components, which indicates that a continuous electronic pathway exists between the fibers and nanostructured carbon domains. Secondly, the magnitude of electrochemical capacitance that is measured in CIOPs while flat or flexed is dramatically larger than the capacitance of the carbon fibers alone. A large electrochemical interface must therefore be present and electrochemically accessible in the form of porous carbon nanoarchitectures that anchor adjacent carbon fibers in CIOPs. Thirdly, galvanostatic charge-discharge tests indicate that the CIOPs continue to store and discharge electrochemical capacitance when cycled at mass-normalized currents of 0.5–2.0 A g^{-1} (Fig. 8). The CIOP electrodes in these

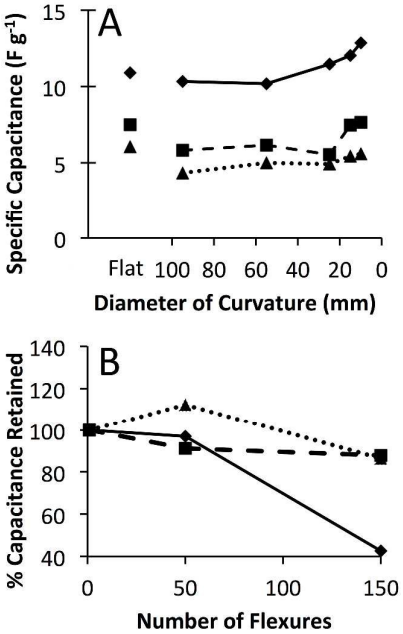

Fig. 7 (A) The magnitude of capacitance measured in 1 M TBAP in acetonitrile for three identically prepared CIOP sheets as a function of their curvature; (B) The percentage of capacitance that is discharged by CIOP sheets after multiple flexures around a 25-mm diameter cylinder.

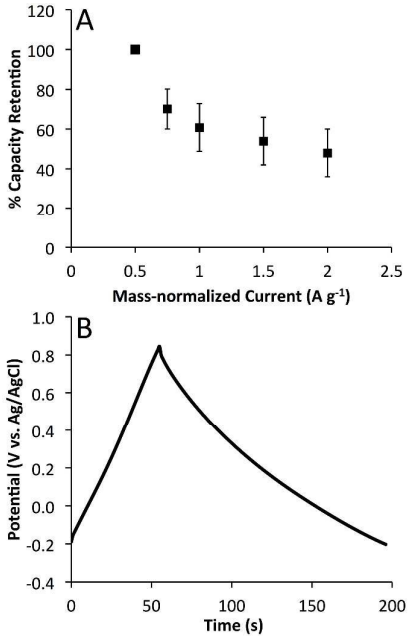

Fig. 8 (A) A plot of the percentage of capacitance that was discharged by CIOP electrodes as they were electrochemically cycled using increasing mass-normalized currents; (B) A plot of the chronopotentiometry data from an CIOP electrode that was charged and discharged at ±0.5 A g^{-1}.

tests typically discharged tens of Farads per gram and continued to discharge 52-69% of their electrochemical capacitance when cycled with a mass-normalized current of 1.0 A g^{-1} and 40-56% at 2.0 A g^{-1}. Like many electrodes, CIOPs increasingly polarize as the reaction rate increases,[40] but it is clear that CIOP electrodes are able to support electrochemical reaction rates that would not be possible on planar electrodes themselves under similar conditions.

As an additional estimate of the rate capability of CIOP electrodes, we created Bode plots of imaginary capacitance from electrochemical impedance data to determine how quickly the maximum amount of electrochemical capacitance discharges from CIOP electrodes. Bode plots display the magnitude of the imaginary component of capacitance that is measured during impedance spectroscopy as a function of the frequency of the alternating current input signal.[33,40,47] The Bode plot of CIOP electrodes reaches a maximum imaginary capacitance at a frequency of ~0.055 Hz, which inversely corresponds to a dielectric relaxation time constant (τ_0) of ~18 s (Fig. 9). For comparison, other porous carbon nanoarchitectures and carbon nanofoam electrodes with >400 m^2 g^{-1} reach peak discharge in similar time frames.[40] This data further supports our interpretation that the carbon inverse opal domains in CIOP electrodes are physically integrated and electrochemically accessible on a meaningful time scale when they are supported on a carbon fiber paper framework. The Bode plot of CIOP electrodes reaches a maximum imaginary capacitance at a frequency of ~0.055 Hz, which inversely corresponds to a dielectric relaxation time constant (τ_0) of ~18 s (Fig. 9). For comparison, other porous carbon nanoarchitectures and carbon nanofoam electrodes with >400 m^2 g^{-1} reach peak discharge in similar time frames.[40] This data further supports our interpretation that the carbon inverse opal domains in CIOP electrodes are physically integrated and electrochemically accessible on a meaningful time scale when they are supported on a carbon fiber paper framework.

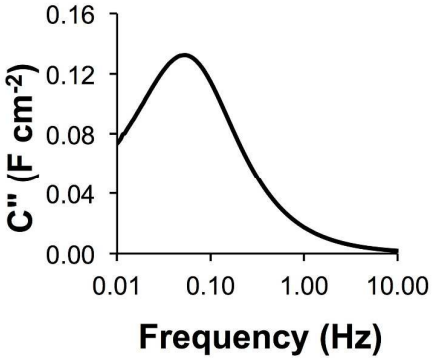

Fig. 9 A Bode plot of a CIOP electrode that was analysed in 2.5 M Li_2SO_4(*aq*) with a direct current bias of 0.2 V at frequencies from 0.01–1×10^6 Hz.

Conclusions

In summary, we report a method to fabricate a new form of carbon inverse opal that merges the nanostructured pore geometry of carbon inverse opal monoliths with the flexibility and conductivity of carbon fiber paper. Integrating carbon fiber papers with nanostructured carbon is not new, but doing so with colloidal crystal templates and carbon inverse opals has not been reported. The resulting CIOPs are vastly more flexible and at least 3 times more electronically conductive than previously published CIOMs. Based on these enhanced properties, this method offers new possibilities for other compositions of inverse opals and nanomaterials that have been primarily prepared as monoliths or powders to be reinvented as components in devices that require flexure and on-board electrochemical reactivity, sensing, and catalysis.

Acknowledgements

We acknowledge Prof. Andreas Stein (University of Minnesota), and Drs. Debra Rolison and Jeffrey Long (U.S. Naval Research Laboratory) for their helpful support of undergraduate research. Acknowledgement is made to the Donors of the American Chemical Society Petroleum Research Fund and to Research Corporation's Cottrell College Science Award program for support of this research.

Notes and references

1 J. Wang, X. Yang, D. Wu, R. Fu, M. S. Dresselhaus and G. Dresselhaus, *J. Power Sources*, 2008, **185**, 589.
2 D. S. Su and R. Schlogl, *ChemSusChem*, 2010, **3**, 136.
3 J. C. Lytle, J. M. Wallace, M. B. Sassin, A. J. Barrow, J. W. Long, J. L. Dysart, C. H. Renninger, M. P. Saunders, N. L. Brandell and D. R. Rolison, *Energy Environ. Sci.*, 2011, **4**, 1913.
4 D. Son, J. Y. Lee, S. Qiao, R. Ghaffari, J. Kim, J. E. Lee, C. Song, S. J. Kim, D. J. Lee, S. W. Jun, S. Yang, M. Park, J. Shin, K. Do, M. Lee, K. Kang, C. S. Hwang, N. Lu, T. Hyeon and D.-H. Kim, *Nat. Nanotechnol.*, 2014, **9**, 397.
5 D. Y. Kang, S. O. Kim, J. K. Lee and J. H. Moon, *Langmuir*, 2013, **29**, 1192.
6 A. A. Zakhidov, R. H. Baughman, Z. Iqbal, C. Cui, I. Khayrullin, S. O. Dantas, J. Marti and V. G. Ralchenko, *Science*, 1998, **282**, 897.
7 K. T. Lee, J. C. Lytle, N. S. Ergang, S. M. Oh and A. Stein, *Adv. Funct. Mater.*, 2005, **15**, 547.
8 F. Su, X. S. Zhao, Y. Wang, J. Zeng, Z. Zhou and J. Y. Lee, *J. Phys. Chem. B*, 2005, **109**, 20200.
9 K. Jurewicz, C. Vix-Guterl, E. Frackowiak, S. Saadallah, M. Reda, J. Parementier, J. Patarin and F. Beguin, *J. Phys. Chem. Solids*, 2004, **65**, 287.
10 C.-Z. Lai, M. A. Fierke, A. Stein and P. Bühlmann, *Anal. Chem.*, 2007, **79**, 4621.
11 G. S. Chai, S. B. Yoon, J.-S. Yu, J.-H. Choi and Y.-E. Sung, *J. Phys. Chem. B*, 2004, **108**, 7074.

12 T. F. Baumann and J. H. Satcher, *J. Non-Cryst. Solids*, 2004, **350**, 120.
13 Z. Wang, F. Li, N. S. Ergang and A. Stein, *Chem. Mater.*, 2006, **18**, 5543.
14 S. Tabata, Y. Isshiki and M. Watanabe, *J. Electrochem. Soc.*, 2008, **155**, K42.
15 Y. Toivola, A. Stein and R. F. Cook, *J. Mater. Res.*, 2004, **19**, 260.
16 R. Petricevic, M. Glora and J. Fricke, *Carbon*, 2001, **39**, 857.
17 J. Wang, M. Glora, R. Petricevic, R. Saliger, H. Proebstle and J. Fricke, *J. Porous Mater.*, 2001, **8**, 159.
18 Y. Y. Diao and X. Y. Liu, in *Adv. Mater. Res.*, eds. J. Shao and Q. Fan, 2012, pp. 183.
19 R. W. Pekala, J. C. Farmer, C. T. Alviso, T. D. Tran, S. T. Mayer, J. M. Miller and B. Dunn, *J. Non-Cryst. Solids*, 1998, **225**, 74.
20 H. Qian, A. R. Kucernak, E. S. Greenhalgh, A. Bismarck and M. S. Shaffer, *ACS Appl. Mater. Interfaces*, 2013, **5**, 6113.
21 W. Dong, J. S. Sakamoto and B. Dunn, *Sci. Technol. Adv. Mater.*, 2003, **4**, 3.
22 T. Liu, T. V. Sreekumar, S. K. Kumar, R. H. Hauge and R. E. Smalley, *Carbon*, 2003, **41**, 2427.
23 T. Bordjiba, M. Mohamedi and L. H. Dao, *J. Electrochem. Soc.*, 2008, **155**, A115.
24 X.-L. Zheng, W.-J. Qin, T. Ling, P. C.-F. and X.-W. Du, *Adv. Mater. Interfaces*, 2015, **2**, 1400464.
25 Z. Liu, Q. Zhang, H. Wang and Y. Li, *Nanoscale*, 2013, **5**, 6917.
26 J. Shao and Q. Fan, *Adv. Mater. Res.*, 2012, **441**, 183.
27 D. Zou, S. Ma, R. Guan, M. Park, L. Sun, J. J. Aklonis and R. Salovey, *J. Polym. Sci. Part A: Polym. Chem.*, 1992, **30**, 137.
28 A. Stein, F. Li and N. R. Denny, *Chem. Mater.*, 2008, **20**, 649.
29 Y. A. Vlasov, X.-Z. Bo, J. C. Sturm and D. J. Norris, *Nature*, 2001, **414**, 289.
30 J. C. Lytle, H. Yan, N. Ergang, W. H. Smyrl and A. Stein, *J. Mater. Chem.*, 2004, **14**, 1616.
31 L. J. van der Pauw, *Philips Res. Rep.*, 1958/59, **20**, 220.
32 M. D. Stoller and S. R. Rodney, *Energy Environ. Sci.*, 2010, **3**, 1294.
33 P. L. Taberna, P. Simon and J. F. Fauvarque, *J. Electrochem. Soc.*, 2003, **150**, A292.
34 K. S. W. Sing, D. H. Everett, R. A. W. Haul, L. Moscou, R. A. Pierotti, J. Rouquerol and T. Siemieniewska, *Pure Appl. Chem.*, 1985, **57**, 603.
35 Y. Liu, S. Gorgutsa, C. Santato and M. Skorobogatiy, *J. Electrochem. Soc.*, 2012, **159**, A349.
36 M. White, E. D. Kaltenbrunner, E. D. Glowacki, K. Gutnichenko, G. Kettlgruber, I. Graz, S. Aazou, C. Ulbricht, D. A. M. Egbe, M. C. Miron, Z. Major, M. C. Scharber, T. Sekitani, T. Someya, S. Bauer and N. S. Sariciftci, *Nature Photonics*, 2013, **7**, 811.
37 D. A. Dikin, S. Stankovich, E. J. Zimney, R. D. Piner, G. H. B. Dommett, G. Evmenenko, S. T. Nguyen and R. S. Ruoff, *Nature*, 2007, **448**, 457.
38 N. Leventis, C. Sotiriou-Leventis, G. Zhang and A.-M. M. Rawashdeh, *Nano Lett.*, 2002, **2**, 957.
39 Y. Qian, A. Vu, W. Smyrl and A. Stein, *J. Electrochem. Soc.*, 2012, **159**, A1135.
40 A. E. Fischer, M. P. Saunders, K. A. Pettigrew, D. R. Rolison and J. W. Long, *J. Electrochem. Soc.*, 2008, **155**, A246.
41 J. W. Long, D. Bélanger, T. Brousse, W. Sugimoto, M. B. Sassin and O. Crosnier, *MRS Bull.*, 2011, **36**, 513.
42 H. A. Andreas and B. E. Conway, *Electrochim. Acta*, 2006, **51**, 6510.
43 Y. Wu, C. Guo, N. Li, L. Ji, Y. Li, Y. Tu and X. Yang, *Electrochim. Acta*, 2014, **146**, 386.
44 S. Biniak, A. Swiatkowski and M. Pakula, in *Chemistry and Physics of Carbon*, ed. L. R. Radovic, Marcel Dekker, New York, 2001.
45 B. E. Conway, *Electrochemical Supercapacitors: Scientific Fundamentals and Technological Applications*, Kluwer Academic Press / Plenum Publishers, New York, NY, 1999.
46 L. Hu, J. W. Choi, Y. Yang, S. Jeong, F. La Mantia, L.-F. Cui and Y. Cui, *PNAS*, 2009, **106**, 21490.
47 C. Portet, P. L. Taberna, P. Simon, E. Flahaut and C. Laberty-Robert, *Electrochim. Acta*, 2005, **50**, 4174.

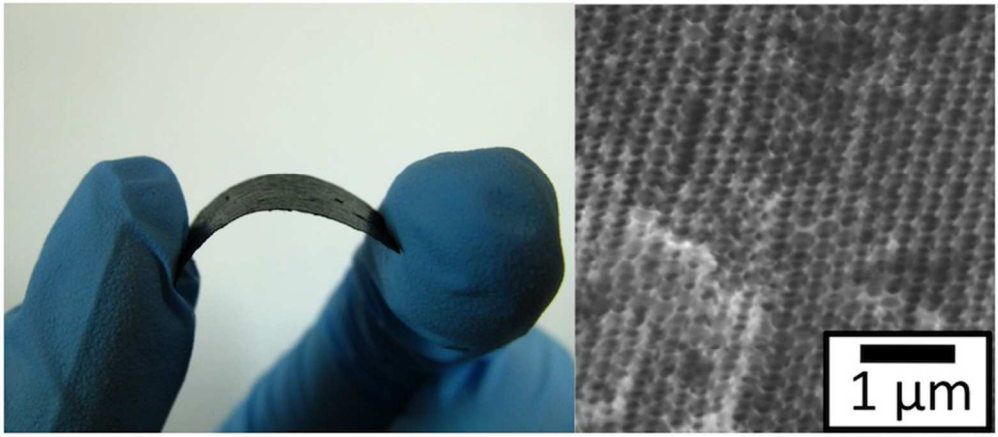

80x35mm (300 x 300 DPI)